JOURNAL OF GEOPHYSICAL RESEARCH, VOL. 103, NO. D1, PAGES 1555-1571, JANUARY 20, 1998

Localized rapid ozone loss in the northern winter stratosphere: An analysis of UARS observations

Hari Nair[1]

Division of Geological and Planetary Sciences, California Institute of Technology, Pasadena

Mark Allen,[2] Lucien Froidevaux, and Richard W. Zurek

Earth and Space Sciences Division, Jet Propulsion Laboratory, Pasadena, California

Abstract. Observations of low-ozone air pockets forming during northern winter in the middle stratosphere outside the polar vortex provide an opportunity to test models of the photochemistry of ozone at several altitudes, as the trajectories of the associated air parcels are well defined by Lagrangian transport codes over the periods of interest, and vertical profiles of key species, including ozone, are available from instruments aboard the Upper Atmosphere Research Satellite (UARS). We find that a Lagrangian photochemical model, where the chemistry within an isolated parcel of air is simulated as it travels along a specified trajectory, does reproduce the observed formation of low-ozone pockets in the 6-10 mbar altitude range within the measurement uncertainties but overestimates the ozone loss rate at higher altitudes. The rapid ozone loss localized in these pockets is due to the isolation of air at high latitudes (and high solar zenith angles). Thus the low ozone levels are due to a decrease in the odd oxygen production rate and not to an increase in the loss rate by reaction with halogen species, as in the "classical" ozone hole.

1. Introduction

The vertical profile of ozone in the terrestrial stratosphere reflects the interaction between dynamics and chemistry. At altitudes above about 35 km, or 6 mbar, ozone is in photochemical steady state. Models of this photochemically controlled region tend to underpredict the abundance of ozone relative to the observations [*World Meteorological Organization (WMO)*, 1986]. This is known as the "ozone deficit" problem, and many studies have been undertaken examining this discrepancy (recent work includes *Eluszkiewicz and Allen* [1993], *Siskind et al.* [1995], and *Crutzen et al.* [1995]). Although most previous efforts concluded that there is a net loss of ozone in the photochemically controlled region above 6 mbar altitude, *Crutzen et al.* [1995] recently used observations from the Upper Atmosphere Research Satellite (UARS) to compute ozone loss rates and showed an apparent net production of ozone relative to the observations above about 2 mbar pressure. *Jucks et al.* [1996] recently used simultaneous measurements of active hydrogen, nitrogen, and chlorine radicals to show that the calculated ozone production and loss rates balance to within 10% from 31 to 38 km altitude (about 10 to 4 mbar), due to measurements of ClO lower than model predictions. Thus there still appears to be some uncertainties surrounding the simulation of chemical processes in current model descriptions.

Since transport is an important factor in determining the ozone concentration at lower altitudes [*Ko et al.*, 1989], it is difficult to test the model chemistry in this region of the atmosphere. Two-dimensional (2-D) photochemical models are typically employed to properly account for the transport of ozone rich air from the tropics to the polar regions [e.g., *Garcia and Solomon*, 1983]. While there is general agreement between such models and observations in this part of the atmosphere, this may be due to the influence of transport, which if improperly parameterized, may obscure errors in the model chemistry.

Rather than looking at seasonal variations of spatially averaged ozone fields, as 2-D models must, a more direct test of model photochemistry in regions of the atmosphere where transport plays an important role is to employ a Lagrangian photochemical model [*Austin et al.*, 1987], where the trajectory of a closed parcel of air (one that does not interact with surrounding air) is explicitly specified by using a Lagrangian transport code. In this case, the net change in species abundances

[1]Now at Hughes Aircraft, Los Angeles, California.

[2]Also at Division of Geological and Planetary Sciences, California Institute of Technology, Pasadena.

Paper number 97JD03072.
0148-0227/98/97JD-03072$09.00

in the parcel is solely due to chemistry. The measurements made by the Microwave Limb Sounder (MLS) onboard UARS of the formation of low-ozone pockets in the northern winter polar midstratosphere [*Manney et al.*, 1995] over periods of a few weeks during December 1992 and late February to March 1993 provide an excellent opportunity to apply such a model.

These low-ozone air pockets are observed to occur during winter when a strong, long-lived anticyclone forms at high latitudes. In the north, such an anticyclone frequently develops in the Pacific sector (i.e., the "Aleutian high"). As indicated by observations made by MLS, tongues of ozone rich air are drawn up from low latitudes and into the anticyclone, sometimes having moved around the polar vortex, which in the north is often displaced away from the pole during these periods. These pathways are confirmed by back trajectories computed for air parcels in the low-ozone pockets, which are localized in the 6-10 mbar altitude range [*Manney et al.*, 1995]. As the air lingers at middle to high latitudes, its ozone mixing ratio is observed to decrease. The pockets of low ozone lingering in the anticyclone have ozone values as much as 3 ppmv lower than the 8 ppmv ozone mixing ratios in the subtropical regions where the air parcels originated.

Morris et al. [1995] and G. A. Morris et al. (unpublished manuscript, 1996) recently investigated the February/March 1993 event with a Lagrangian photochemical model. The conclusion was that air in the low-ozone pockets at the 850 K potential temperature level is isolated at high latitudes for periods of time comparable to the photochemical lifetime of ozone, defined as the ratio of the concentration of ozone to its loss rate. Since the odd oxygen production rate is low at high latitudes, the ozone abundance drops as it relaxes to the photochemical equilibrium value. Air outside the pockets at similar latitudes meanders back and forth between middle and high latitudes over short timescales compared to the lifetime of odd oxygen. Consequently the average odd oxygen production rate remains relatively high, and the ozone mixing ratio does not fall to low values. The role of the anticyclone is to cause the air to linger at high latitudes while keeping it from moving downward and into the polar vortex.

In this paper, we undertake a more comprehensive study of the December 1992 and February/March 1993 events, using a Lagrangian photochemical model to simulate the time dependent ozone loss rates within parcels of air following specific trajectories leading to the observed low-ozone pockets and within parcels leading to neighboring regions with higher ozone. Furthermore, we do this at several different heights, extending our initial study [*Nair et al.*, 1995]. In this computation of loss rates, we have utilized measurements taken by the MLS and the cryogenic limb etalon array spectrometer (CLAES) instruments along these trajectories to better constrain the abundances of species involved in the chemical destruction of ozone. Discrepancies between the observed and the predicted ozone loss rates will highlight uncertainties in the standard gas phase photochemistry.

The abundances of the active hydrogen, nitrogen, and chlorine radicals that participate in the catalytic cycles which destroy odd oxygen in the stratosphere may be determined by either direct measurements or inferred from measurements of other species. *Jackman et al.* [1986] incorporated O_3, H_2O, HNO_3, NO_2, and temperature data from the limb infrared monitor of the stratosphere (LIMS) to compute ozone production and loss rates. *Froidevaux et al.* [1989] also used LIMS observations of H_2O, NO_2, and temperature to constrain the abundances of HO_x and NO_x radicals in the calculations of the ozone profile above 6 mbar. Similar approaches have been taken using data from both LIMS and ATMOS [e.g., *Natarajan et al.*, 1986; *Callis et al.*, 1986; *McElroy and Salawitch*, 1989; *Allen and Delitsky*, 1991a]. In this paper, the stratospheric abundance of odd hydrogen (HO_x) radicals is constrained by simultaneous MLS measurements of water vapor and ozone. The active nitrogen and chlorine budgets are constrained by CLAES observations of HNO_3 and $ClONO_2$, along with estimates of total NO_y ($= NO + NO_2 + NO_3 + HNO_3 + 2N_2O_5 + ClONO_2$) and Cl_y ($= Cl + ClO + HCl + ClONO_2$) made from the observed abundances of tracer species such as N_2O or CH_4 from CLAES [e.g., *Fahey et al.*, 1990; *Plumb and Ko*, 1992; *Woodbridge et al.*, 1995]. The following section describes the spacecraft instruments and the measurements.

2. UARS Observations of Trace Species

The Microwave Limb Sounder instrument has three radiometers that measure emission from the atmospheric limb at 63, 183, and 205 GHz [*Barath et al.*, 1993]. The 63 GHz radiometer provides information on pressure and temperature based on O_2 emission, the 183 GHz radiometer measures emission from H_2O and O_3, and the 205 GHz radiometer measures bands of ClO and O_3. In the 1 to 10 mbar altitude range, the 205 GHz ozone retrievals have an estimated precision and accuracy of 0.2 to 0.3 ppmv, which is better than 10% at 1 mbar and better than 5% at 10 mbar. The 183 GHz retrievals are less accurate due to the poorer characterization of the 183 GHz ozone band. We have employed maps made from the 205 GHz measurements (version 3) for this work. Validation of the MLS ozone measurements is discussed more fully by *Froidevaux et al.* [1996].

The validation of the H_2O measurements is described by *Lahoz et al.* [1996]. In the 1 to 10 mbar range of interest the single profile precision is 0.1 to 0.2 ppmv (better than 4%), and the accuracy is 0.5 to 0.7 ppmv, or better than 10%.

Observations of chlorine monoxide (ClO) are also available from MLS [*Waters et al.*, 1996]. Unfortu-

nately, the data are quite noisy; the typical single profile noise at the 1σ level ranges from 0.4 ppbv at 10 mbar to 1.2 ppbv at 1 mbar. Typical model peak mixing ratios of ClO for the air parcels we consider here are of the order of 0.4 ppbv or less. Given the large uncertainties in the single profile values of ClO and its short photochemical lifetime, we do not assimilate these observations but instead allow the model to compute ClO.

CLAES also measures emission spectra at the atmospheric limb, and is further described by *Roche et al.* [1993]. Validated data products from CLAES include CH_4, N_2O, HNO_3, and $ClONO_2$. The quality of CH_4 and N_2O measurements are discussed by *Roche et al.* [1996]. In the 3-15 mbar range, CLAES CH_4 appears to be systematically 15 to 25% too high relative to correlative measurements. CLAES N_2O agrees to within 20% with correlative measurements, with no clear systematic bias as with CH_4. Random errors for each gas are of the order of 5-10%.

The validation of the HNO_3 measurements is discussed by *Kumer et al.* [1996]. In the current version of the CLAES data (version 7), HNO_3 appears to be underestimated relative to correlative measurements by 15-25% at low mixing ratios (below 8 ppbv). For this reason we have increased the observed HNO_3 mixing ratios by 20% at all altitudes before assimilating them into the model.

The validation of $ClONO_2$ measurements is described by *Mergenthaler et al.* [1996]. Although the uncertainties are of the order of 20% below 10 mbar altitude, above this level, interference by other gases (chiefly O_3 and CO_2) becomes appreciable and the uncertainty approaches 100% at 6 mbar. We have incorporated the observations of $ClONO_2$ into the model for trajectories ending at the 740 K and 840 K levels, since these trajectories remain at higher pressures than 6 mbar for the most part. Calculations along trajectories ending at the 960 K potential temperature level do not assimilate $ClONO_2$ measurements but instead allow the model to determine $ClONO_2$.

3. Lagrangian Photochemical Model

We have adapted the Caltech/JPL photochemical model [*Allen and Delitsky*, 1991b] to operate in a Lagrangian mode, similar to the work of *Austin et al.* [1987], *Jones et al.* [1990], and *Kawa et al.* [1993]. In this mode of calculation the chemistry of an isolated air parcel with a specified trajectory is simulated, accounting for changes in temperature, pressure, radiation field, and other relevant physical parameters as warranted by the path of travel. Since we have decoupled the chemistry and dynamics, the observed rate of ozone loss is solely due to photochemical processes. In this case, the continuity equation simply becomes

$$\frac{\partial n_i}{\partial t} = P_i - L_i$$

where n is the number density of species i, and P_i and L_i are the chemical production and loss terms, respectively, for species i. The data set of reactions and photochemical cross sections, partially shown in Table 1, is taken mostly from the 1994 JPL evaluation [*DeMore et al.*, 1994].

Back trajectory calculations are run using winds from the United Kingdom Meteorological Office (UKMO) troposphere-stratosphere data assimilation system [*Swinbank and O'Neill*, 1994]. The validity of these back trajectory calculations was demonstrated by showing that long-lived tracers, particularly N_2O as observed by CLAES, are generally conserved along these paths during the periods when the low-ozone pockets develop [*Manney et al.*, 1995].

Parcel positions (longitude, latitude, and pressure) are computed at noon UT at each day over the period of the trajectory. Profiles of ozone at the computed parcel positions are generated for noon UT from synoptic maps (as described by *Elson and Froidevaux* [1993], a map of observations interpolated to a common universal time). Temperature profiles at these times are also derived from UKMO data. The radiation field is computed assuming a spherical atmosphere. The solar flux is taken from *Mentall et al.* [1981] and *Mount and Rottman* [1982].

The full model atmosphere consists of 40 levels from the surface to 0.316 mbar, which is the vertical range of the UKMO analyses. The parcel is placed in the middle of the grid, and the continuity equation for each species is solved only at this level. The other levels are used for a precise calculation of the radiation field. Levels are evenly spaced in the logarithm of pressure between the surface and the level of the parcel and also between the level of the parcel and the topmost level at 0.316 mbar. The photochemical model time step is 1 hour except at twilight (within an hour of sunrise or sunset), where it is taken to be 10 min. At the beginning of each time step, the position of the parcel (longitude, latitude, log pressure) is found by linear interpolation between the positions in the trajectory code output. The local solar time of the parcel is also updated to account for motion in longitude. The vertical gridding of the atmosphere is recalculated at each time step with the assumption of hydrostatic equilibrium to account for vertical motion of the parcel. Updated ozone and temperature profiles are also constructed by linear interpolation. Mixing ratios of O_2, N_2, O_3, H_2O, N_2O, HNO_3, and CH_4 are constrained to follow the observed quantities, as described in the following section. Concentrations of all other species in the model (Table 2) are computed from the continuity equation. Mixing ratios of all species at each level are assumed to be conserved as the density changes.

We will compare the computed changes in ozone with the observed changes. The net production rate of odd oxygen per day is computed by summing the rates of all reactions in the model which either produce or destroy

Table 1. Important Reactions for Odd Oxygen Balance

Number	Reaction	ΔO_x	Number	Reaction	ΔO_x
(R1)	$O_2 + h\nu \rightarrow 2\,O$	+2	(R147)	$N + NO \rightarrow N_2 + O$	+1
(R2)	$O_2 + h\nu \rightarrow O + O(^1D)$	+2	(R148)	$N + NO_2 \rightarrow N_2O + O$	+1
(R5)	$HO_2 + h\nu \rightarrow OH + O$	+1	(R149)	$NO + O + M \rightarrow NO_2 + M$	−1
(R8)	$H_2O + h\nu \rightarrow 2\,H + O$	+1	(R150)	$NO + O_3 \rightarrow NO_2 + O_2$	−1
(R10)	$NO + h\nu \rightarrow N + O$	+1	(R158)	$NO_2 + O_3 \rightarrow NO_3 + O_2$	−1
(R11)	$NO_2 + h\nu \rightarrow NO + O$	+1	(R166)	$NO_3 + O \rightarrow O_2 + NO_2$	−1
(R12)	$NO_3 + h\nu \rightarrow NO_2 + O$	+1	(R193)	$O + OClO \rightarrow ClO + O_2$	−1
(R16)	$N_2O_5 + h\nu \rightarrow NO + NO_3 + O$	+1	(R194)	$O + OClO + M \rightarrow ClO_3 + M$	−1
(R24)	$ClO + h\nu \rightarrow Cl + O$	+1	(R195)	$O + Cl_2O \rightarrow 2\,ClO$	−1
(R25)	$ClOO + h\nu \rightarrow ClO + O$	+1	(R196)	$O + ClNO_3 \rightarrow O_2 + ClONO$	−1
(R26)	$OClO + h\nu \rightarrow ClO + O$	+1	(R197)	$O + HCl \rightarrow OH + Cl$	−1
(R36)	$ClNO_3 + h\nu \rightarrow O + ClONO$	+1	(R198)	$O + HOCl \rightarrow OH + ClO$	−1
(R83)	$CO_2 + h\nu \rightarrow CO + O$	+1	(R199)	$O(^1D) + Cl_2 \rightarrow Cl + ClO$	−1
(R95)	$2\,O + M \rightarrow O_2 + M$	−2	(R200)	$O(^1D) + HCl \rightarrow Cl + OH$	−1
(R99)	$O + O_3 \rightarrow 2\,O_2$	−2	(R201)	$O(^1D) + HCl \rightarrow ClO + H$	−1
(R102)	$O(^1D) + O_3 \rightarrow 2\,O_2$	−2	(R202)	$O(^1D) + CHFCl_2 \rightarrow CFCl_2 + OH$	−1
(R104)	$O + H_2 \rightarrow OH + H$	−1	(R203)	$O(^1D) + CHF_2Cl \rightarrow CF_2Cl + OH$	−1
(R105)	$O + OH \rightarrow O_2 + H$	−1	(R204)	$O(^1D) + CCl_4 \rightarrow CCl_3 + ClO$	−1
(R106)	$O + HO_2 \rightarrow OH + O_2$	−1	(R205)	$O(^1D) + CFCl_3 \rightarrow CFCl_2 + ClO$	−1
(R107)	$O + H_2O_2 \rightarrow OH + HO_2$	−1	(R206)	$O(^1D) + CF_2Cl_2 \rightarrow CF_2Cl + ClO$	−1
(R108)	$O(^1D) + H_2 \rightarrow H + OH$	−1	(R207)	$O(^1D) + CF_3Cl \rightarrow CF_3 + ClO$	−1
(R109)	$O(^1D) + H_2O \rightarrow 2\,OH$	−1	(R217)	$O(^1D) + CF_3CFCl_2 \rightarrow Cl + 4\,F + ClO$	−1
(R112)	$H + O_3 \rightarrow OH + O_2$	−1	(R219)	$O(^1D) + COCl_2 \rightarrow 2\,ClO + CO$	−1
(R115)	$H + HO_2 \rightarrow H_2O + O$	+1	(R220)	$O(^1D) + COFCl \rightarrow ClO + FCO$	−1
(R116)	$2\,OH \rightarrow H_2O + O$	+1	(R259)	$Cl + O_3 \rightarrow ClO + O_2$	−1
(R118)	$OH + O_3 \rightarrow HO_2 + O_2$	−1	(R313)	$ClO + O \rightarrow Cl + O_2$	−1
(R122)	$HO_2 + O_3 \rightarrow OH + 2\,O_2$	−1	(R315)	$ClO + O_3 \rightarrow OClO + O_2$	−1
(R125)	$O + NO_2 \rightarrow NO + O_2$	−1	(R316)	$ClO + O_3 \rightarrow ClOO + O_2$	−1
(R126)	$O + NO_2 + M \rightarrow NO_3 + M$	−1	(R331)	$OClO + O_3 \rightarrow ClO + 2\,O_2$	−1
(R127)	$O + HNO_3 \rightarrow OH + NO_3$	−1	(R353)	$O + ClCO \rightarrow Cl + CO_2$	−1
(R128)	$O + HO_2NO_2 \rightarrow OH + NO_2 + O_2$	−1	(R358)	$O + ClCO_3 \rightarrow Cl + O_2 + CO_2$	−1
(R129)	$O + N_2O_5 \rightarrow 2\,NO_2 + O_2$	−1	(R491)	$O + CH_4 \rightarrow CH_3 + OH$	−1
(R130)	$O(^1D) + N_2 + M \rightarrow N_2O + M$	−1	(R494)	$O + H_2CO \rightarrow OH + HCO$	−1
(R131)	$O(^1D) + N_2O \rightarrow 2\,NO$	−1	(R496)	$O(^1D) + CH_4 \rightarrow CH_3 + OH$	−1
(R132)	$O(^1D) + N_2O \rightarrow N_2 + O_2$	−1	(R497)	$O(^1D) + CH_4 \rightarrow CH_3O + H$	−1
(R133)	$O_3 + CH_3ONO \rightarrow CH_3ONO_2 + O_2$	−1	(R498)	$O(^1D) + CH_4 \rightarrow H_2CO + H_2$	−1
(R143)	$N + O_2 \rightarrow NO + O$	+1	(R532)	$CH_3 + O \rightarrow H_2CO + H$	−1
(R144)	$N + O_3 \rightarrow NO + O_2$	−1	(R535)	$CH_3 + O_3 \rightarrow CH_3O + O_2$	−1

Table 2. Species in Photochemical Model

O	$O(^1D)$	H	H_2	OH	HO_2
H_2O_2	N	NO	NO_2	NO_3	N_2O_3
N_2O_4	N_2O_5	HNO	HNO_2	HO_2NO_2	CH_3ONO
CH_3ONO_2	$CH_3O_2NO_2$	Cl	Cl_2	ClO	ClOO
OClO	ClO_3	Cl_2O	Cl_2O_2	Cl_2O_3	ClNO
$ClNO_2$	ClONO	$ClNO_3$	HCl	HOCl	CH_2Cl
CCl_3	$CFCl_2$	CF_2Cl	CH_3Cl	CH_2FCl	$CHFCl_2$
CHF_2Cl	CCl_4	$CFCl_3$	CF_2Cl_2	CH_3CCl_3	CF_3CCl_3
CF_3CFCl_2	ClCO	CHClO	$COCl_2$	COFCl	CH_2ClO
CH_3OCl	CH_2ClO_2	CCl_3O_2	$CFCl_2O_2$	CH_2ClO_2H	O_2ClNO_3
CCl_3NO_4	$CFCl_2NO_4$	CH_3	CO	CO_2	HCO
H_2CO	CH_2OH	CH_3O	CH_2O_2	CH_2OOH	CH_3OH
CH_3O_2	CH_3OOH	$HOCH_2OO$			

odd oxygen (defined as the sum of O, $O(^1D)$, and O_3), as listed in Table 1. ΔO_x is the net change in odd oxygen per reaction [*Johnston and Podolske*, 1978; *Allen et al.*, 1984].

4. Assimilation of UARS Data

The chemical composition of the parcel is initialized to be consistent with UARS observations. The total NO_y and Cl_y budgets are initialized according to piecewise linear fits made to Figures 6 and 7 in the work of *Plumb and Ko* [1992]. We assume that the parcel is in photochemical equilibrium for the initial latitude in the trajectory file. Since there is some scatter in the NO_y relation, we will use both a high and a low NO_y value, as shown in Figure 1. The high NO_y value is more appropriate for tropical air, whereas the low value is more appropriate for midlatitude air (see Figure 6 of Plumb and Ko).

Similar correlations between CH_4 and NO_y, as well as Cl_y, have also been noted (M. Gunson and R. Salawitch, private communication, 1995). The predicted NO_y and Cl_y from the CH_4 relations agree fairly well with the predictions from the N_2O relations, once the observed CH_4 mixing ratio is reduced to account for the measurement bias described earlier.

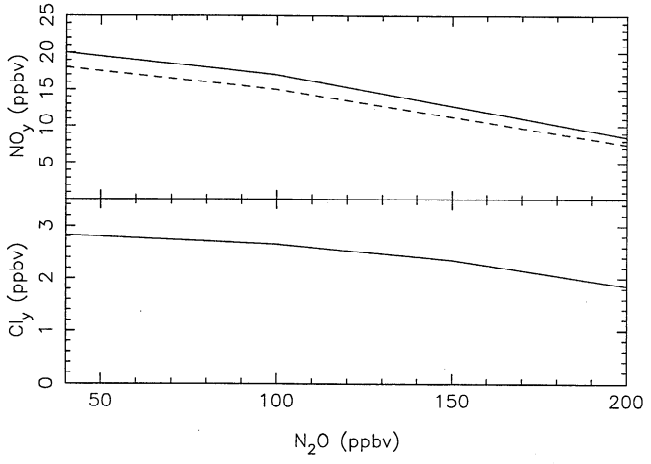

Figure 1. Total NO_y and Cl_y as a function of N_2O. The top panel shows high (solid line) and low (dashed) total NO_y as a function of N_2O. The bottom panel shows total Cl_y.

In order to determine the partitioning between members of the active nitrogen and chlorine families at the start of the run, all of the NO_y and Cl_y is assumed initially to be in the form of HNO_3 and HCl, respectively. The abundances of O_2, N_2, and O_3 are fixed to their initial values. All other species concentrations are computed self-consistently. The parcel is held at the latitude, pressure, and season at which it originated for 3 weeks of model time, long enough for the partitioning between members in the active nitrogen and chlorine families to reach a diurnally varying photochemical equilibrium.

Observations of trace gases (O_3, H_2O, N_2O, HNO_3, CH_4, and $ClONO_2$) made by UARS instruments over the period of interest have been assimilated into the photochemical model. Using the proper ozone profile is important since models of the terrestrial stratosphere have generally underpredicted ozone abundances in the photochemically controlled region above 35 km altitude [*Eluszkiewicz and Allen*, 1993]. The chemical destruction rate of ozone is itself dependent on the ozone concentration. Thus in order to compute the loss rate without introducing potential errors related to the ozone deficit problem, the observed ozone concentration in the parcel should be used. A second-order effect is the sensitivity of the radiation field to the ozone profile, which impacts the abundances of active radical species.

The concentrations of long-lived species (H_2O, N_2O, HNO_3, and CH_4) in the parcel are updated at each time step in the same manner as the ozone abundance. Concentrations are found by linear interpolation in time between concentrations taken from maps made for noon UT for each day over the period of the trajectory. The abundances of the long-lived species are not otherwise allowed to vary.

Short-lived species that have significant diurnal variations (in this case $ClONO_2$) must be treated differently. Because of the nature of the UARS orbit, any particular latitude is observed at two local times per day: once during the ascending track and once during the de-

scending track. Two $ClONO_2$ concentration maps are produced for each day over the time period of the trajectory; one is made by using only ascending track observations, and one is made from only descending track observations. Each latitude on each map thus has one specific local time associated with it. Mixing ratios of $ClONO_2$ at the parcel location are assimilated into the model twice per day at the local times corresponding to the parcel latitude; at one local time the observation is read off the map made by using only ascending track observations, at the other the observation is read from the map made from descending track observations.

By updating HNO_3 and $ClONO_2$ in this manner, we have added artificial sources (or sinks) for NO_y and Cl_y. In order to conserve the total amount of active nitrogen, each day at noon UT the concentrations of all of the NO_y species besides HNO_3 are uniformly increased (or decreased) by a common factor in order to keep the total NO_y amount equal to the initial NO_y inventory of the parcel. Using this procedure, we find that the total abundance of active nitrogen computed by the model changes by no more than 10% over the course of a day. Twice each day when $ClONO_2$ is updated, HCl and ClO are also increased (or decreased) by a common factor in order to keep the total Cl_y constant. The model predicts a negligible change in the total Cl_y between the twice daily updates.

5. Simulation of February/March 1993 Event

5.1. Baseline Model Results

Figure 2 shows two vertical profiles of ozone taken from a synoptic map generated from MLS observations for noon UT, March 7, 1993. The dashed line is inside the low-ozone pocket at 258.5° east longitude and 67.5° north latitude. The solid line shows the vertical profile of ozone outside the pocket at 178.5° east longitude and 67.5° north latitude. Note that the ozone peak in the pocket is lower and sharper than for the ozone peak outside the pocket and that the ozone in the pocket is considerably depleted relative to the ozone outside from about 1-10 mbar. The nature and history of these low-ozone pockets is described more fully by *Manney et al.* [1995].

We have computed the chemical evolution of parcels along several different trajectories ending at the 740, 840, and 960 K potential temperature levels at the position of the pocket (corresponding to 14.7, 10.4, and 7.1 mbar, respectively, on March 7), and also at the 840 K level outside the pocket (11.3 mbar) at the same latitude. We will compare the magnitudes and trends of the observed and modeled ozone loss rates in parcels leading to the low-ozone pocket as well as for parcels with trajectories ending outside the low-ozone pocket, where the ozone has "normal" values with the observed changes in ozone along the computed trajectories. Disagreement between the observed and the predicted ozone loss rates will reflect uncertainties in the model chemistry.

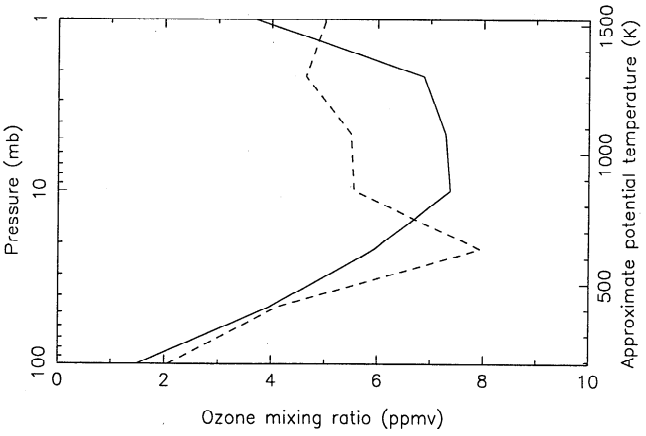

Figure 2. Ozone profiles inside (dashed line) and outside the pocket (solid line) on March 7, 1993. Both profiles are at 67.5° north latitude.

The trajectories ending in the low-ozone pockets are described by *Manney et al.* [1995]; trajectories ending outside the pockets are calculated in a similar manner. The trajectory model was run backward in time for 22 days, starting at 1200 UT, March 7, 1993, and ending February 14, 1993. The first group of trajectories was initialized on the 740, 840, and 960 K isentropic surfaces on a 0.5° by 0.5° latitude longitude grid, running from 230° to 279.5° east longitude and 56° to 71.5° north latitude. A second run for air outside the pocket, with ozone values more representative of the zonal mean, was made for the same dates and latitude range but from 150° to 199.5° east longitudes. We have simulated the chemistry along five trajectories ending in a cluster within the pocket at each of the 740 K, 840 K, and 960 K levels and at 840 K outside the pocket, as shown in Figure 3. Note that the trajectories ending at the position of the pocket begin at lower latitudes, where ozone abundances are high.

Uncertainties in the trajectory model are difficult to quantify. These errors manifest themselves not only by affecting the physical conditions of the parcel (solar zenith angle, pressure, temperature) but also in the initialization and assimilation of spatially variable species. As a conservative estimate of the cumulative uncertainty in parcel position on February 14, 1993, which is the end of the back calculation started on March 7, 1993, we take the uncertainty to be 5° in longitude, 2.5° in latitude, and 30 K in potential temperature. We will employ this "uncertainty box" to estimate the errors in mixing ratios of ozone and other species along the trajectory.

To initialize the NO_y and Cl_y partitioning, the latitude, pressure, and solar longitude are fixed to their values at noon UT February 14, 1993, for each trajectory. The mean N_2O mixing ratio in the cluster of parcels ending at 840 K within the pocket is approxi-

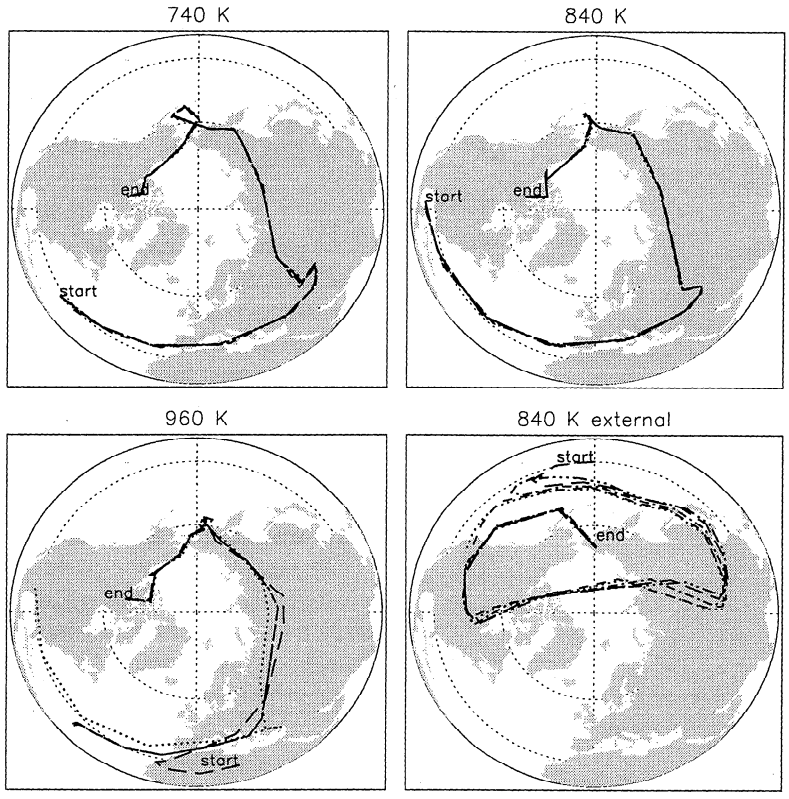

Figure 3. Four sets of trajectories for the February/March 1993 event. Each group contains five distinct parcels, ending in a cross pattern with the parcel centers separated by 0.5°. Parcel positions are plotted at noon UT for each day from February 14, 1993, to March 7, 1993. The parcels drawn into the anticyclone show a net counterclockwise motion about the pole because the anticyclone as a whole moves in an eastward direction, as seen in Figure 2 of *Manney et al.* [1994].

mately 120 ppbv. We have initialized the parcels with 15.6 ppbv NO_y and 2.55 ppbv Cl_y based on the high NO_y curve of Figure 1. Calculations made by using the low NO_y correlation will be addressed in a later section. The mixing ratios of O_2, N_2, and O_3 are fixed to their initial values (20.9%, 78.1%, and 9.1 ppmv, respectively). All other species are computed self-consistently for 3 weeks of model time such that the members of the NO_y and Cl_y families converge to a diurnally repeating photochemical steady state.

Figure 4a shows the average observed ozone abundance along the 840 K trajectories leading to the pocket. The ozone values have been smoothed by replacing each point with the average of the point and its two neighbors, keeping the endpoints unchanged. This makes it easier to see trends in the day-to-day change in the measured ozone. The second panel compares the day-to-day change in the smoothed ozone (triangles) with the model predictions for change in ozone (circles) over the period of the trajectories. We estimate the minimum uncertainty on the observed day-to-day change in the ozone mixing ratio to be of the order of 0.4 ppmv; since the precision of individual MLS ozone measurements is of the order of 0.2 ppmv. Note that this uncertainty is, in most cases, larger than the magnitude of the day-to-day change! Nonetheless, there is an obvious long-term trend in the observations, and both the observed and the model ozone changes are systematically negative and of roughly the same magnitude, with the notable exception of days 50 through 55, where the model ozone loss is greater than the observed loss. The observed overall decrease in ozone is 3.4 ppmv with an estimated uncertainty of 0.9 ppmv, based on the variation of observed ozone mixing ratios in our "uncertainty box." The integrated model loss is 3.6 ppmv. The third and fourth panels show the average pressure and latitude histories of the parcels, respectively. The fourth panel also shows the average noontime solar zenith angle of the parcels as a function of time, which is a measure of the solar radiation received.

Figure 5 is a similar plot for the trajectories leading to the point outside the pocket at 840 K. The ozone mixing ratio remains relatively constant over this time period, although a gentle oscillation with a period of about a week can be seen. The observed change in ozone over the 3 week period of the trajectory is a slight increase of 0.4 ± 0.5 ppmv, while the model predicts a decrease of 1.4 ppmv. Although the agreement between the model

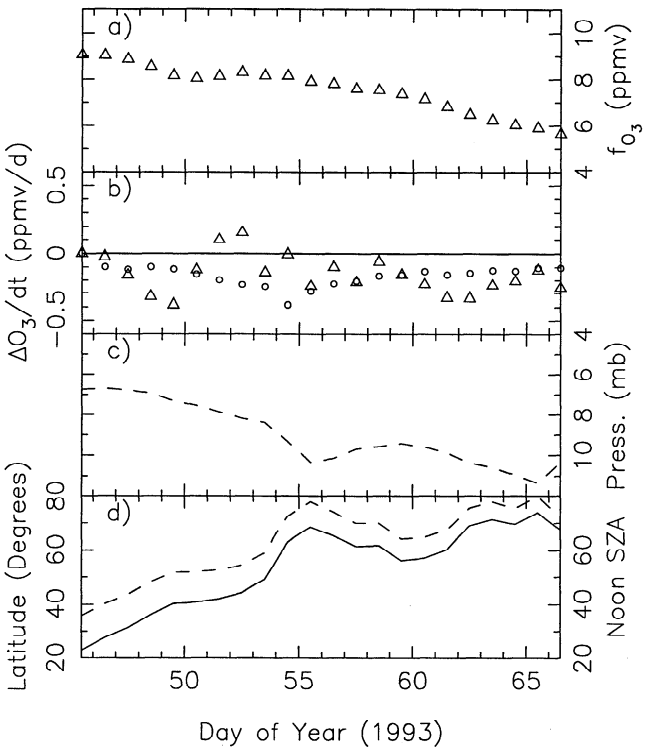

Figure 4. Average ozone loss over the 840 K trajectories leading to the pocket. The observed loss is 3.4 ± 0.9 ppmv and the model loss is 3.6 ppmv. (a) Ozone mixing ratio as observed by the Microwave Limb Sounder (MLS); (b) observed change in ozone (triangles), model calculation with standard chemistry (circles); (c) pressure; (d) latitude (solid line) and noontime solar zenith angle (dashed) of the parcels as a function of time.

and the observations is poor for this case, both values are significantly smaller than for the trajectories leading to the pocket.

Figure 6 shows the model results at the 740 K potential temperature level within the pocket. Note the large drop in the observed ozone over the first few days of the trajectories. This leads us to suspect that the trajectories may be in error for this time period. Looking at the average mixing ratios of the long-lived tracers for these parcels (Figure 7), we note considerable variability over the first 10 days of the trajectories. Thus these particular trajectories probably do not describe the true motion of these parcels, at least before day 55. Over the last 10 days or so, the model is in better agreement (except for the last day). However, it must still be noted that both the model and the observed changes in ozone are small (~ 0.1 ppmv) over the last 10 days compared to the uncertainty on the observed day-to-day change (0.3 ppmv).

Finally, Figure 8 summarizes the history of the parcels ending within the pocket at the 960 K potential temperature level. Note in the second panel that the model ozone losses are consistently much greater than the observations would indicate. In fact, the integrated model loss of ozone is 13.4 ppmv, greater than the initial abundance! This unphysical result occurs because the computed loss rates are based on the observed ozone mixing ratio, which is fixed to match the observed quantity in the model calculations. The model predictions for the day-to-day changes come into much better agreement near the end of the trajectory, as the parcels descend to around 7 mbar. This is interesting because the ozone deficit generally manifests itself in photochemical models at altitudes above about 6 mbar. These parcels appear to move from an altitude where there is an ozone deficit to one where there is not, reflected in the second panel. We show three sets of computed ozone losses; the solid circles are computed by using the low NO_y mixing ratios and the asterisks show the computed ozone loss with low NO_y and a modified value for the reaction of OH and ClO. Calculations with modified chemistry will be addressed in a later section.

The results we have presented thus far do show a qualitatively interesting point, namely that the model ozone deficit still appears to exist above about 7 mbar altitude, while the model appears to predict changes in ozone below this altitude reasonably accurately. However, as we have seen for all of the cases shown above, there are many uncertainties. For example, individual trajectories may not properly describe the true air motion, particularly near the end of the back trajectory (day 45), or the initialization of species in the parcels may be wrong.

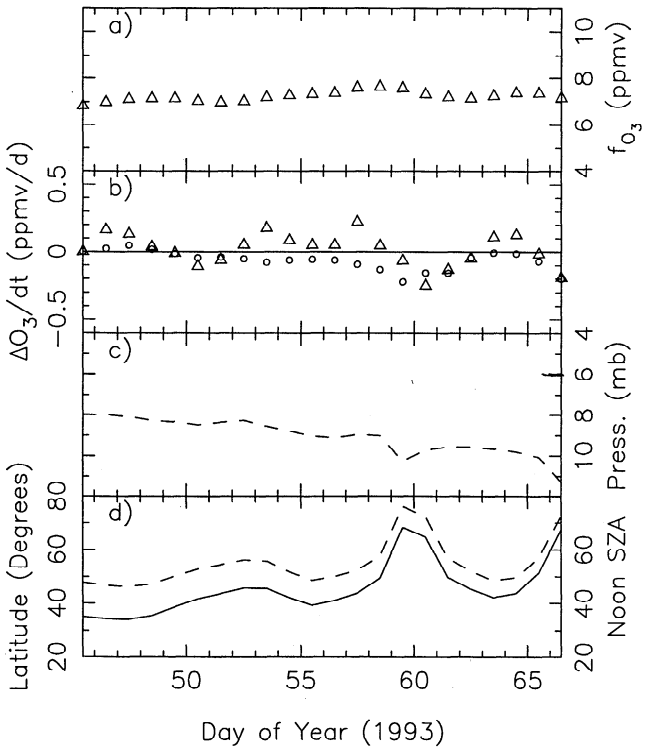

Figure 5. As Figure 4 but for the trajectories ending outside the pocket. The observed change in ozone is 0.4 ± 0.5 ppmv and the model change is -1.4 ppmv.

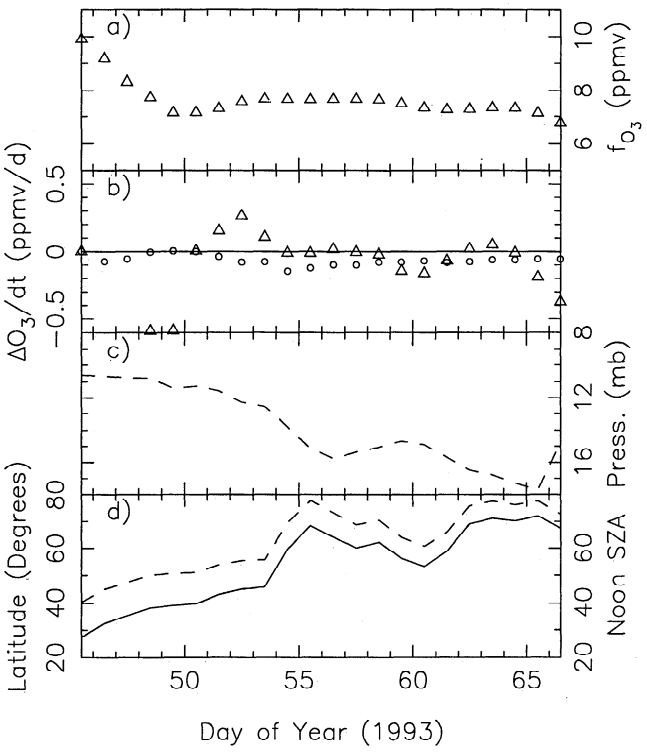

Figure 6. As Figure 4 but for the parcels ending at 740 K within the pocket. The observed change in ozone is -3.2 ± 1.8 ppmv and the model change is -1.4 ppmv.

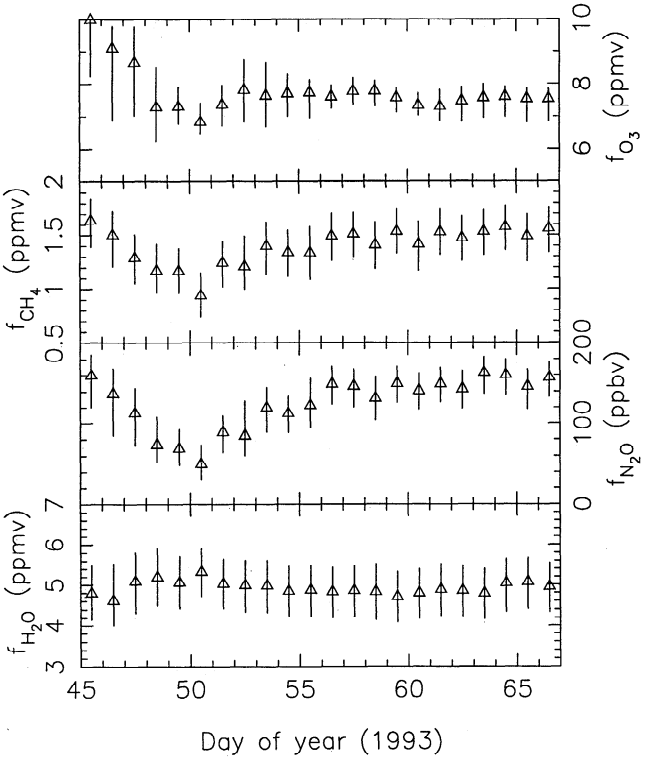

Figure 7. Mixing ratios of O_3 and the long-lived tracer species CH_4, N_2O, and H_2O along the 740 K trajectories.

Figure 9 compares the simulated daily changes in ozone with the observed daily changes in each group of trajectories. Each group has (5 trajectories)*(22 points/trajectory) = 110 points in it. We have plotted the average of the day-to-day changes for each group along with the sample standard deviation. Note that the predicted ozone decreases for parcels ending at 960 K are all much greater than the observed losses. It must be noted that this is a relatively small sample size and more cases should be run before quantitative conclusions may be drawn. However, it does appear that the model adequately describes the chemistry in the parcels below about the 840 K potential temperature level and consistently overpredicts ozone loss rates above this.

5.2. Influence of Vertical and Latitudinal Motion on Ozone Loss Rates

A trajectory has three components, motion in longitude, motion in latitude, and motion in pressure. Since the motion in longitude has a small effect on the solar zenith angle, compared to the rotation of the Earth, motion in latitude and pressure have a much larger impact on changing the radiation field, which in turn drives the processes that produce and destroy ozone. We have seen from the 960 K runs in the previous section that the pressure at which the parcel is located potentially has a large effect on the computed ozone loss rate. Thus it is worthwhile to distinguish the effects of motion in pressure and latitude on the loss rate of ozone.

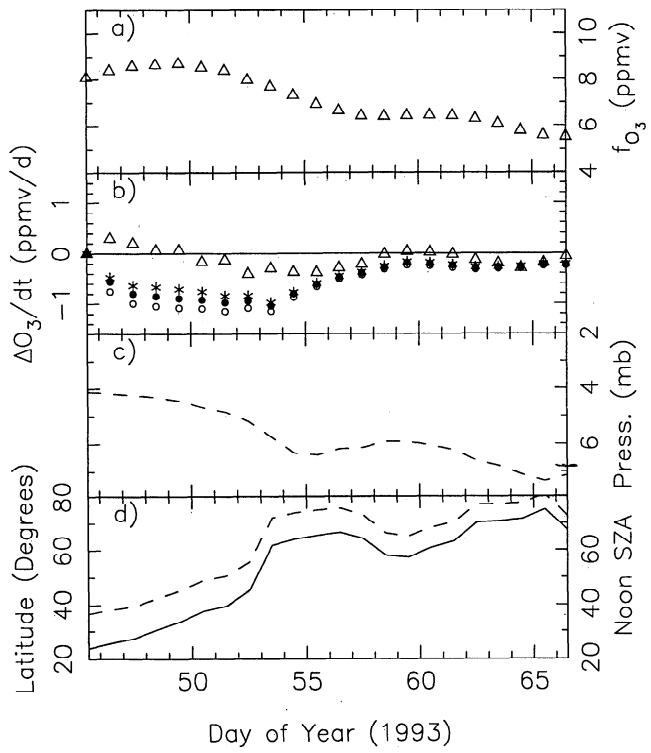

Figure 8. As Figure 4 but for the parcels ending at 960 K within the pocket. The observed change in ozone is -2.6 ± 0.6 ppmv and the model change is -13.4 ppmv. Figure 8b shows model loss with standard chemistry (open circles), low NO_y (solid circles), and low NO_y plus modified chlorine chemistry (asterisks).

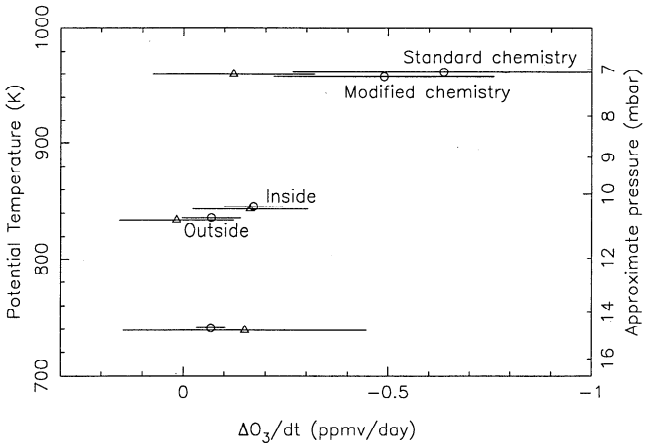

Figure 9. Average model (circles) versus observed (triangles) daily changes in ozone over the period of the trajectories. Points are slightly offset from the 740, 840, and 960 K potential temperature levels for ease of visualization. The error bars extend out to one sample standard deviation in each direction.

We have performed a series of numerical experiments where we examine the effects on the ozone abundance of individually varying the pressure and latitude over one of the trajectories shown in the last section ending at the 840 K level within the pocket. In each model run, we either allow the pressure and/or latitude to vary according to the computed trajectory (shown in Figures 4c and 4d) or fix them to their initial values (6.74 mbar and 22.9° north, respectively). In these calculations we allow the model to compute the abundances of all species, including ozone, self-consistently. Since these are fictitious trajectories, it is not appropriate to assimilate measurements from the actual trajectory. The chemical initialization for each parcel is the same as for the 840 K trajectory in the previous section. The computed ozone mixing ratios and total change in ozone for each case are shown in Figure 10.

We see that allowing the pressure to vary over the range traversed by the parcel produces a negligible change in the ozone mixing ratio from the cases where the pressure is held fixed (Figures 10a and 10b). However, allowing the latitude to vary produces a large change in ozone, comparable to the observed change along the actual trajectory (Figures 10c and 10d). In each case, the mixing ratio of ozone in the parcel relaxes toward a photochemical equilibrium value, where the odd oxygen production and loss rates are equal. This photochemical equilibrium value is lower closer to the pole, because of the lower solar illumination and hence lower oxygen photolysis rate. In Figures 10a and 10b, where the latitude is fixed at 22.9°, the equilibrium value of ozone is about 8 ppmv. In Figures 10c and 10d, where the parcel rapidly moves northward and stays poleward of 60° for most of the last 10 days, the equilibrium value is around 5 ppmv. Note that when both pressure and latitude are varied appropriately (Figure 10d), the calculated ozone change of -3.6 ppmv compares well with the observed change of -3.4 ppmv.

Now consider the two parcels ending at 840 K inside and outside the pocket. From Figures 4 and 5 the parcels follow similar pressure paths but very different latitude paths, although the final latitude is 67.5° north in each case. The noontime solar zenith angle is greater than 60° for the last 12 days or so for the parcel ending within the pocket (Figure 4d), while the noontime solar zenith angle mostly remains below 60° for the parcel ending outside the pocket (Figure 5d). In each case, the production of odd oxygen is anticorrelated with the noontime solar zenith angle (which increases as the parcel nears the pole). For the parcel ending outside the pocket, there is a slight net production of odd oxygen at low latitudes as the ozone concentration in the parcel is below the low-latitude equilibrium value. Conversely, at high latitudes, there is a net loss of ozone. The ozone mixing ratio in parcels rapidly moving between these two regions reflects a balance between the average production and the loss over periods comparable to the photochemical lifetime of ozone, which is about 10 days at 35 km altitude [*Ko et al.*, 1989]. Figure 10e shows

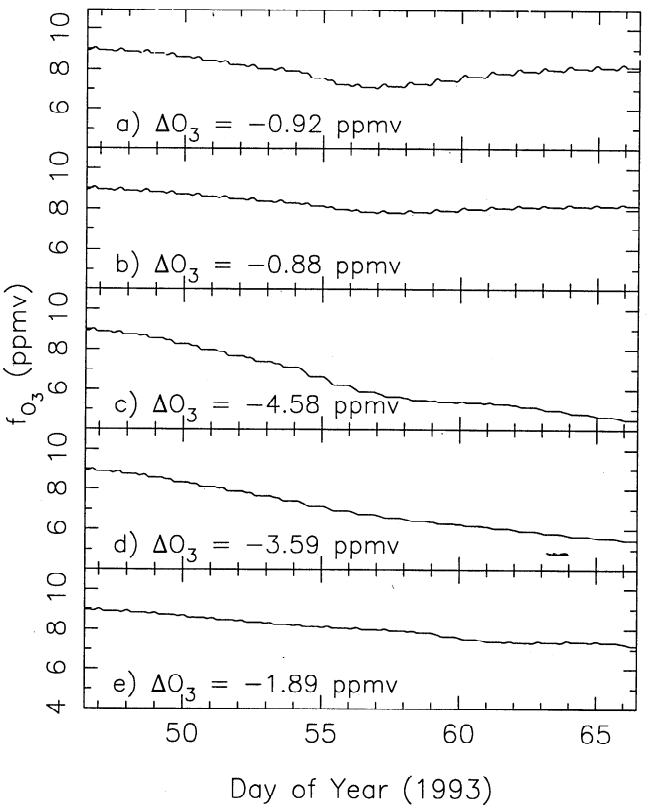

Figure 10. Computed ozone mixing ratios for five cases: (a) pressure = 6.74 mbar, latitude = 22.9°; (b) pressure varies according to Figure 4c, latitude = 22.9°; (c) pressure = 6.74 mbar, latitude varies according to Figure 4d; (d) vary pressure and latitude according to Figures 4c and 4d; (e) vary pressure and latitude according to Figures 5c and 5d.

the calculated ozone change for a parcel following the trajectory ending at the 840 K potential temperature level outside the low-ozone pocket, with the same chemical initialization as in Figures 10a-10d. The calculated ozone loss is 1.9 ppmv, much smaller than the loss along the trajectory leading to the pocket. Thus the varying concentration of ozone in air parcels at the latitudes of the low-ozone pockets reflects different exposure times to sunlight as the parcels take different paths through the higher latitudes.

G. A. Morris et al. (unpublished manuscript, 1996) performed numerical experiments to examine the effects of varying the trajectory followed by a parcel on its ozone content. Their findings are consistent with those presented here: that the low-ozone pockets form in the middle stratosphere when air is held at high latitudes for a week or more and that air outside the anticyclone does not exhibit these low-ozone values as it is not confined to high latitudes. Adjusting other factors, such as temperature and the initial values of ozone and NO_y, in their model did not have an appreciable effect on the final ozone mixing ratios.

5.3. Uncertainties in NO_y and Cl_y

We have seen in the previous section that the ozone loss rates over the trajectories ending at the 840 K level can be qualitatively explained by the change in solar radiation received at the parcel location, in the sense that high noontime solar zenith angles correlate with large ozone losses. On the other hand, when the parcel is at altitudes where the model ozone deficit becomes a problem (early in the trajectories ending at the 960 K level), high model ozone loss rates occur with low noontime solar zenith angles. In this section we will consider possible contributors to the model ozone deficit.

Most of the ozone loss is due to a small number of reactions, namely the reaction of atomic oxygen and ozone as well as the loss due to the catalytic cycles

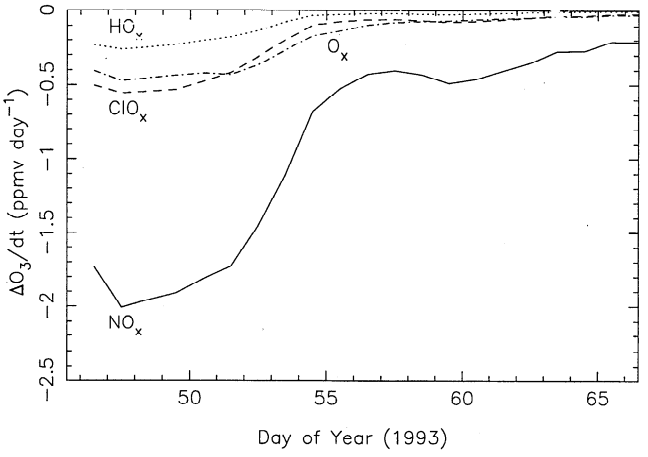

Figure 11. Daily integrated odd oxygen loss rates due to NO_x, ClO_x, O_x, and HO_x over a February/March 1993 trajectory ending at 960 K.

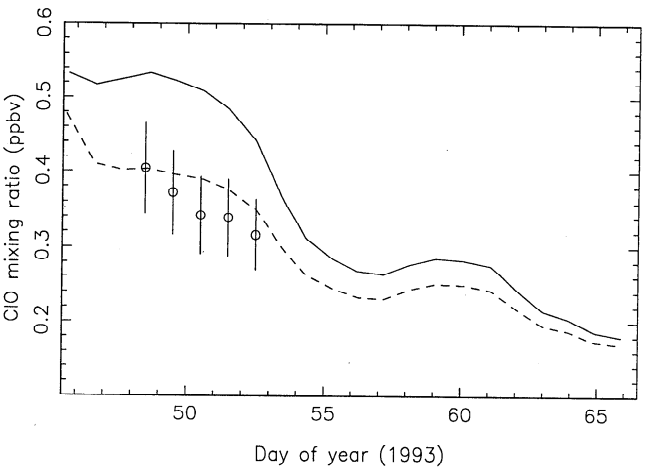

Figure 12. Model daily maximum ClO mixing ratios using standard chemistry (solid line) and modified chlorine chemistry (dashed) for a 960 K parcel. The symbols represent MLS zonal mean ClO interpolated to the latitude and pressure of the parcel, along with the estimated 15% measurement uncertainty. Refer to Figure 8c for the latitude and pressure history of the parcel. MLS zonal means northward of 50° are not shown due to lack of zonal symmetry.

involving the NO_x, ClO_x, and HO_x families, given by

$$L = 2k_{99}[O][O_3] + 2k_{106}[O][HO_2] + 2k_{125}[O][NO_2] + 2k_{313}[O][ClO],$$

where the k_n values are the reaction rate coefficients we have employed in our model (see Table 1). Figure 11 shows the integrated daily loss rates for each of the main contributors to the ozone loss along a trajectory ending at 960 K.

The major sink of odd oxygen is the catalytic destruction by NO_x, comprising 70% of L along the whole trajectory. As mentioned earlier, the $N_2O - NO_y$ correlation we use is based on Figure 6 of *Plumb and Ko* [1992], which has some scatter, particularly at N_2O values around 50 ppbv. All of the model runs presented thus far have employed the higher NO_y distribution (solid line of Figure 1, top panel), which is appropriate for parcels originating from the tropics (equatorward of 30°). In this section, we will consider cases where the parcels are initialized with the lower NO_y distribution, with consequently lower NO_x-induced ozone loss.

Another possible candidate for the high model ozone losses is an overabundance of active chlorine. Over the course of the 22 day trajectory the catalytic loss due to ClO_x is as much as 20% of L and is the second most important loss channel in the first several days where the parcel is above 5 mbar. *Michelsen et al.* [1995] showed that the partitioning of Cl_y in current photochemical models does not agree with observations below 50 km altitude. The ClO/HCl ratio is overpredicted by as much as a factor of 3 near 40 km altitude, which results in a greater degree of ozone loss in the mod-

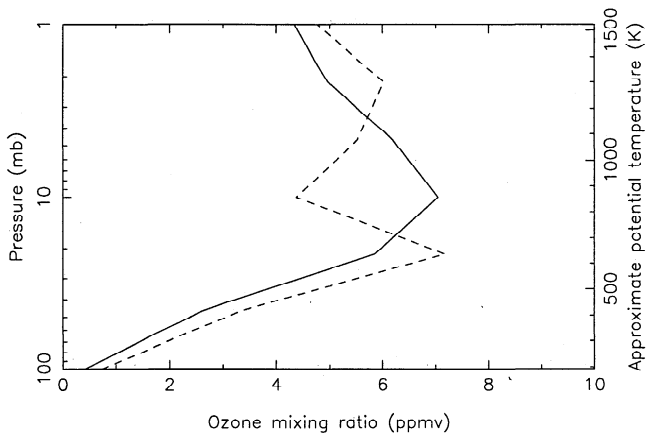

Figure 13. Ozone profiles inside (dashed line) and outside the pocket (solid line) on December 24, 1992. Both profiles are at 47.5° north latitude.

els. *Dessler et al.* [1996] showed that model ClO is a factor of 2 higher than MLS measurements obtained from February to March 1993 between 40 and 46 km altitude. *Michelsen et al.* [1995] found that incorporation of a 7% production yield of HCl from the reaction of ClO and OH markedly increases the agreement between the modeled and the observed Cl_y partitioning. The work of *Jucks et al.* [1996] also strongly supports the existence of an additional HCl source.

We have made model runs at the 960 K level with the low NO_y distribution and the 7% HCl branch. The relative partitioning between NO_y species at the start of the run is assumed to be the same as in the high NO_y case. The initial partitioning between chlorine species was found by running the model to steady state with the 7% HCl branch at the initial parcel latitude. The agreement between the model daily maximum ClO and the zonal mean value from MLS observations (interpolated to the appropriate longitude and pressure) is greatly improved after the incorporation of the new ClO + OH reaction up to about day 54, where the parcel is located between 4 and 5 mbar (Figure 12). After this the parcel remains at high latitudes where zonal means are not particularly meaningful due to the pronounced zonal asymmetry.

Figure 8b shows the net change (production minus loss, or $P - L$) in ozone over the parcel trajectories ending at 960 K for the standard case, low NO_y, and low NO_y plus the modified OH + ClO reaction. We find only slight improvement in the agreement between modeled and observed ozone loss rates, as shown in Figure 9. Decreasing the NO_y and ClO contribute roughly equally to reducing the net ozone loss at high altitudes. Although the combination of the low NO_y and 7% HCl branch causes a considerable decrease in the magnitude of $P - L$ relative to the standard case, particularly in the early part of the trajectory when the parcel is higher

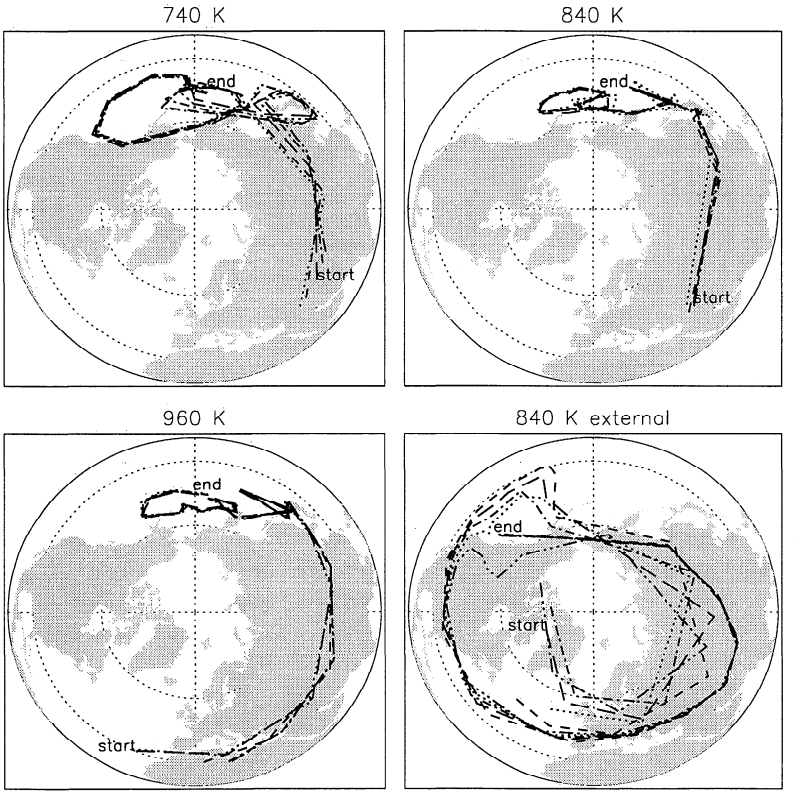

Figure 14. Four sets of trajectories for the December 1992 event. Trajectories begin December 3, 1992, and end December 24, 1992.

than the 5 mbar altitude level, the model and observed $P - L$ still differ by up to 1 ppmv/d. Since the magnitude of the contribution to the ozone loss from odd chlorine is near or below 0.5 ppmv/d (Figure 11), it is unlikely that additional modifications in the chlorine chemistry will resolve the imbalance in the production and loss for this trajectory. There still appears to be a clear discrepancy between model and observed ozone chemistry in the upper stratosphere.

Jucks et al. [1996] used simultaneous measurements taken in September 1989 at 34° north of active hydrogen, nitrogen, and chlorine radicals to show that the calculated ozone production and loss rates balance to within 10% from the 10 to 4 mbar altitude levels. At the present time we have no explanation for the discrepancy between their findings and ours, namely that model error in the Cl_y partitioning does not appear to be entirely responsible for the 960 K ozone deficit.

6. Simulation of December 1992 Event

A low-ozone pocket was also seen in December 1992, however, the latitude of formation was not so near the pole; the center of the pocket was located at about 45° north as opposed to about 65° north latitude for the February/March 1993 event. Figure 13 shows observed vertical profiles of ozone inside the pocket (174.5° east, 47.5° north) and outside the pocket (229.5° east, 47.5° north) on December 24, 1992. Again, the ozone at the position of the pocket has a low, sharp peak and is considerably depleted relative to the external profile at the 10 mbar level.

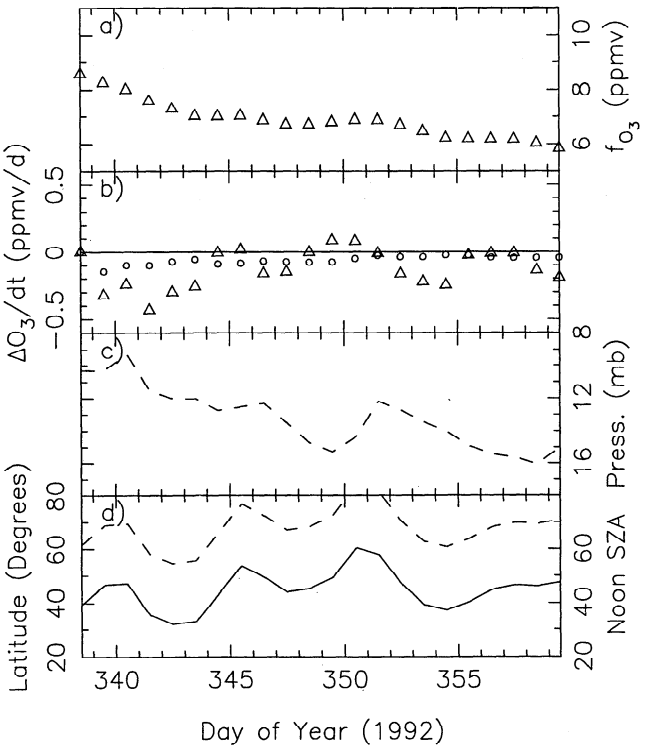

Figure 15. As Figure 4 but for the trajectories ending at 740 K inside the pocket during the December 1992 event. The observed change in ozone is -2.7 ± 1.1 ppmv and the model change is -1.3 ppmv.

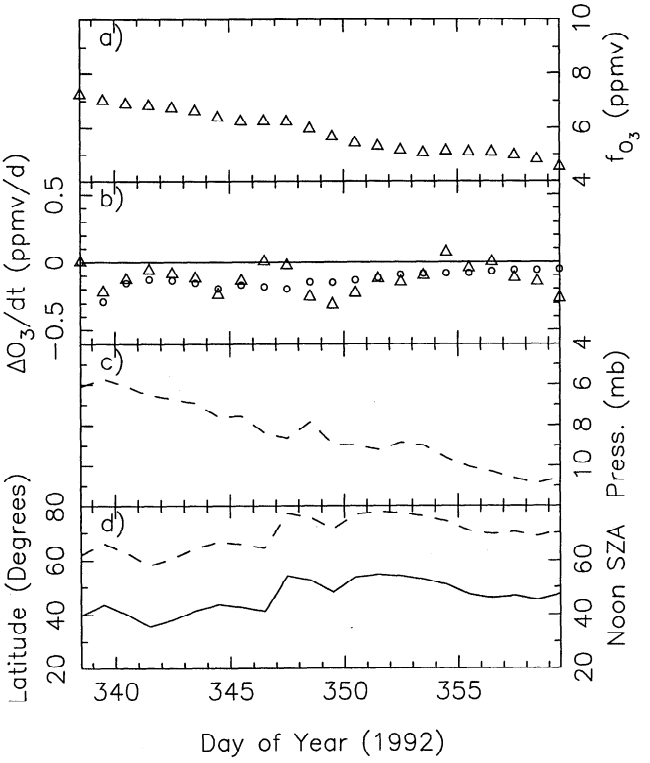

Figure 16. As Figure 15 but for the trajectories ending at 840 K inside the pocket. The observed change in ozone is -2.7 ± 0.6 ppmv and the model change is -2.7 ppmv.

As with the February/March 1993 event, the ozone loss rates along trajectories leading to both inside and outside the pocket were computed. Figure 14 shows the calculated trajectories for five parcels ending at each of the 740, 840, and 960 K potential temperature levels within the pocket (corresponding to 15.0, 10.6, and 7.0 mbar, respectively, on December 24) and for five parcels ending at the 840 K potential temperature level outside the pocket (10.6 mbar). The trajectories for this event differ from the February/March 1993 event since the air parcels leading to the pocket stay close to 45° north latitude for most of the period of the trajectory. Although the latitude of this event was about 20° lower than for the February/March 1993 event, the noontime solar zenith angles were actually slightly greater since this event occurred close to the northern winter solstice (see Figures 15–18).

Figures 15 and 16 show the average observed ozone mixing ratio, observed and calculated loss rates, pressure, latitude, and noon solar zenith angle for the parcels ending at the 740 and 840 K potential temperature levels, respectively, for the December 1992 event. The computed model loss of 1.3 ppmv is smaller in magnitude than the observed decrease of 2.7 ± 1.0 ppmv

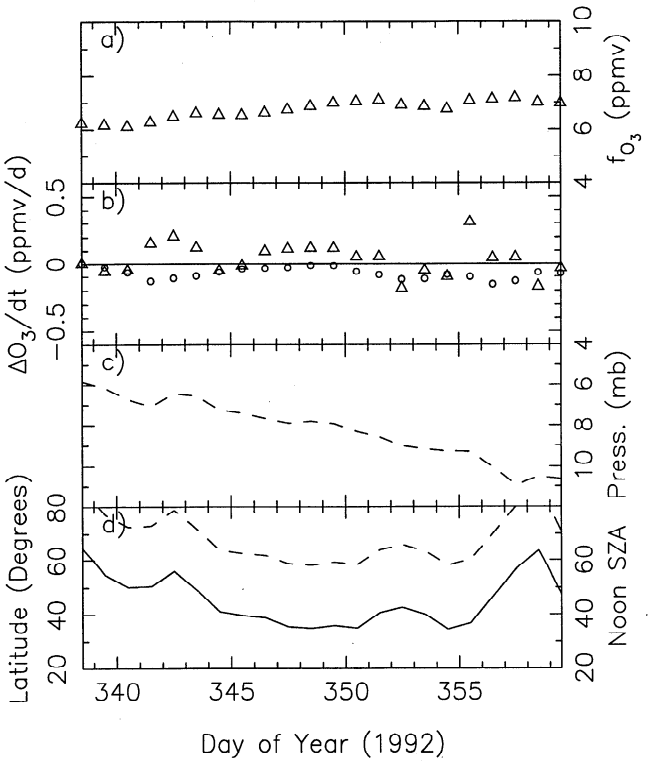

Figure 17. As Figure 15 but for the trajectories ending at 840 K outside the pocket. The observed change in ozone is 0.7 ± 0.4 ppmv and the model change is -1.6 ppmv.

for the 740 K trajectory. The integrated model ozone loss of 2.7 ppmv is in good agreement with the observed ozone loss of 2.7 ± 0.6 ppmv for the 840 K trajectory.

Figure 17 is a similar plot for the trajectories which end at the 840 K level outside the pocket. As with the February/March 1993 event, the observed ozone mixing ratio increases over the period of the trajectory (by 0.7± 0.4 ppmv), while the model predicts a decrease of 1.6 ppmv. Note that the average noontime solar zenith angle for the parcels leading to the pocket (Figure 16d) is greater than for the parcels ending outside of the pocket (Figure 17d) after day 345 for about 10 days, which is comparable to the photochemical lifetime of ozone at this altitude. As a consequence of the reduced solar illumination over a period of this timescale, both the observed and the predicted ozone losses should be much larger for the trajectories leading to the pocket. The parcels ending outside the pocket are subjected to higher solar zenith angles over the last three days of the model simulation, but there is no decrease in ozone since this is a short period of time compared to the photochemical lifetime of ozone. Thus it appears that the same processes which produce a low-ozone pocket at high latitudes also operate at lower latitudes.

The 960 K results are summarized in Figure 18. We find that the model prediction of 6.2 ppmv for the integrated ozone loss exceeds the average observed losses of 1.9 ± 0.4 ppmv for parcels ending at the 960 K potential temperature level, although the discrepancy is not so great as for the February/March 1993 case. This is because the ozone mixing ratios in the parcel over the period of the trajectory were lower than for the February/March 1993 event [*Manney et al.*, 1995], which leads to smaller loss rates. Even so, there remains a serious discrepancy between observed and modeled loss rates, particularly in the early part of the trajectories where the parcels are above about 6 mbar.

Figure 18b also shows the computed daily ozone losses with low NO_y and low NO_y plus the modified OH + ClO reaction. The integrated losses in these cases were 5.1 and 4.5 ppmv, respectively. Again, although the agreement between the observed and the modeled ozone losses is improved, the model still overestimates the ozone loss, particularly at lower pressures early in the trajectory. In this instance the model also overestimates the ClO mixing ratio early in the trajectory, compared to the zonal mean ClO measurements from MLS (Figure 19), unlike the good agreement found in the other event. Thus even with the 7% branch for HCl production, the description of chlorine chemistry in the model is still in error. If we extrapolate the effect of lowering ClO on the integrated ozone loss, we estimate that lowering ClO by another 20% to agree with the MLS zonal means would equivalently reduce the magnitude of the computed integrated ozone loss by 20%,

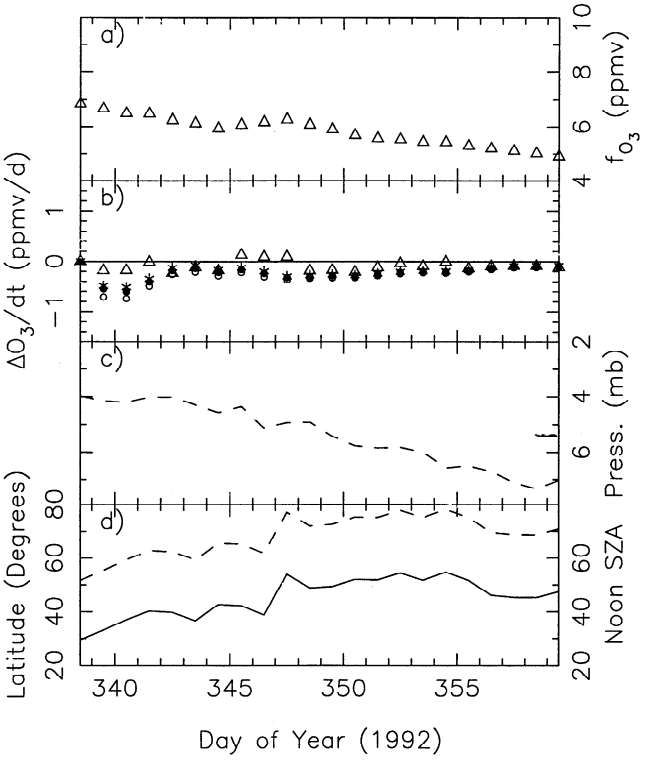

Figure 18. As Figure 15 but for the trajectories ending at 960 K within the pocket. The observed change in ozone is −1.9 ± 0.4 ppmv and the model change is -6.2 ppmv. Computations with modified chemistry are also shown, in the same fashion as Figure 8.

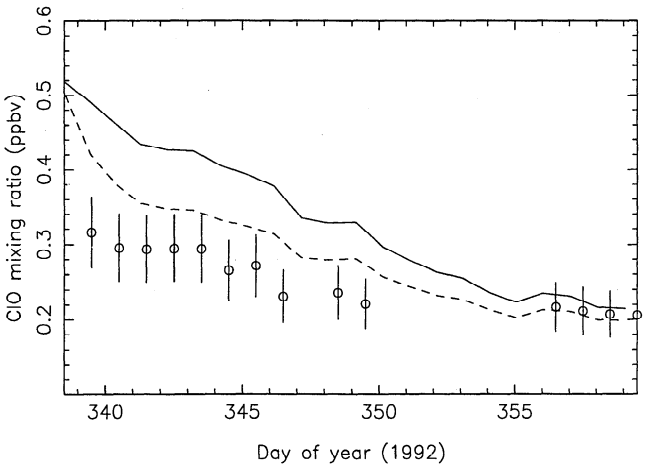

Figure 19. Model daily maximum ClO mixing ratios using standard chemistry (solid line) and modified chlorine chemistry (dashed) for a 960 K parcel. The symbols represent MLS zonal mean ClO interpolated to the latitude and pressure of the parcel, along with the estimated 15% measurement uncertainty. Refer to Figure 18 for the latitude and pressure history of the parcel. MLS zonal means northward of 50° are not shown due to lack of zonal symmetry.

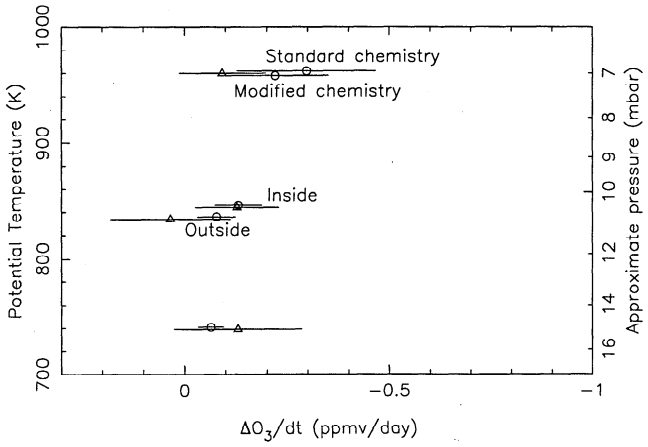

Figure 20. Average model (circles) versus observed (triangles) daily changes in ozone over the period of the trajectories. Points are slightly offset from the 740, 840, and 960 K potential temperature levels for ease of visualization. The error bars extend out to one sample standard deviation in each direction.

or to about 3.5 ppmv, still leading to a discrepancy between the observed (1.9 ± 0.4 ppmv) and the computed integrated ozone losses.

Figure 20 summarizes the comparison between the observed daily changes in ozone with the model changes similar to Figure 9. Like the February/March 1993 event, we find that the model agrees well with the observed loss rates at the lower altitudes, but the model overestimates the loss rate at the highest altitude. Incorporation of lower NO_y abundances and the 7% production yield of HCl from ClO + OH does lead to better agreement between the model and the observed ozone loss rates, although this agreement is at the extreme ranges of the uncertainties.

7. Conclusions

We have investigated the chemical evolution of specific parcels of air along trajectories computed by *Manney et al.* [1995] leading to observed pockets of extravortical, ozone poor air in the middle stratosphere in February/March 1993 and December 1992. These pockets of air occur in an altitude region where both dynamics and chemistry are important contributors to the ozone budget. Observations of trace species from the Microwave Limb Sounder (MLS) and the cryogenic limb array etalon spectrometer (CLAES) aboard the Upper Atmosphere Research Satellite (UARS) were incorporated into a Lagrangian photochemical model to test whether the description of photochemical processes in current models accurately determines the rate of ozone loss near the 740, 840, and 960 K potential temperature levels.

Trajectory calculations for both events indicate that when air is held at high solar zenith angles for periods of time longer than the photochemical lifetime of ozone, a low-ozone pocket forms. Since the photolysis rate of oxygen at high solar zenith angles is small, ozone mixing ratio falls to low values in order for the loss rate to balance the production of odd oxygen. Air outside of these pockets and outside the polar vortex typically swings back and forth between middle and high latitudes such that the average production rate of odd oxygen is high relative to that of air in the low-ozone pocket. Thus the steady state ozone mixing ratio for this "normal" air is higher than the mixing ratios found in the vortex and the low-ozone pockets. The low-ozone levels for parcels outside the polar vortex are due to the longer residence times of these parcels at higher latitudes and the corresponding decrease in the odd oxygen production rate and not to an increase in the loss rate by reaction with halogen or other species. These findings are consistent with the conclusions of G. A. Morris et al. (unpublished manuscript, 1996).

At altitudes below about 7 mbar the photochemical model satisfactorily reproduces the observed ozone loss. However, we find that the photochemical model consistently overestimates the loss rate for ozone at pressures less than about 7 mbar. This is a region of the atmosphere where models have historically overpredicted ozone loss rates relative to production (the "ozone deficit"). In contrast to earlier work, we find that adjusting the chlorine partitioning does not definitively resolve this issue above the 960 K potential temperature level. Thus it appears that significant uncertainties remain in our understanding of the photochemical processes controlling ozone in the upper stratosphere.

Acknowledgments. We would like to thank Gloria Manney for providing trajectories for this effort. We would also like to thank Gloria Manney for her comments and Gary Morris for providing a prepublication manuscript of his work. This work was carried out in part at the Jet Propulsion Laboratory, California Institute of Technology, and was supported as part of UARS guest and theoretical investigations.

References

Allen, M., and M. L. Delitsky, Inferring the abundances of ClO and HO_2 from Spacelab 3 Atmospheric Trace Molecule Spectroscopy observations, *J. Geophys. Res., 96,* 2913–2919, 1991a.

Allen, M., and M. L. Delitsky, A test of odd-oxygen photochemistry using Spacelab 3 Atmospheric Trace Molecule Spectroscopy observations, *J. Geophys. Res., 96,* 12883–12891, 1991b.

Allen, M., J. I. Lunine, and Y. L. Yung, The vertical distribution of ozone in the mesosphere and lower thermosphere, *J. Geophys. Res., 89,* 4841–4872, 1984.

Austin, J., R. C. Pallister, J. A. Pyle, A. F. Tuck, A. M. Zavody, Photochemical model comparisons with LIMS observations in a stratospheric trajectory coordinate system, *Q. J. R. Meteorol. Soc., 113,* 361–392, 1987.

Barath, F. T., et al., The Upper Atmosphere Research Satellite Microwave Limb Sounder instrument, *J. Geophys. Res., 98,* 10751–10762, 1993.

Callis, L. B., M. Natarajan, R. E. Boughner, J. M. Russell III, and J. D. Lambeth, Stratospheric photochemical studies using Nimbus 7 data, 2, Development of inferred trace specie distributions, *J. Geophys. Res., 91,* 1167–1197, 1986.

Crutzen, P. J., J.-U. Grooß, C. Brühl, R. Müller, and J. M. Russell III, A reevaluation of the ozone budget with HALOE UARS data: No evidence for the ozone deficit, *Science, 268,* 705–708, 1995.

DeMore, W. B., S. P. Sander, D. M. Golden, R. F. Hampson, M. J. Kurylo, C. J. Howard, A. R. Ravishankara, C. E. Kolb, and M. J. Molina, Chemical kinetics and photochemical data for use in stratospheric modeling, in *Evaluation 11, JPL Publ. 94-26,* Jet Propul. Lab., Pasadena, Calif., 1994.

Dessler, A. E., S. R. Kawa, D. B. Considine, J. W. Waters, L. Froidevaux, and J. B. Kumer, UARS measurements of ClO and NO_2 at 40 and 46 km and implications for the model "ozone deficit," *Geophys. Res. Lett., 23,* 339–342, 1996.

Elson, L. S., and L. Froidevaux, The use of Fourier transforms for asynoptic mapping: Early results for the Upper Atmosphere Research Satellite Microwave Limb Sounder, *J. Geophys. Res., 98,* 23,039–23,049, 1993.

Eluszkiewicz, J. E., and M. Allen, A global analysis of the ozone deficit in the upper stratosphere and lower mesosphere, *J. Geophys. Res., 98,* 1069–1082, 1993.

Fahey, D. W., S. Solomon, S. R. Kawa, M. Loewenstein, J. R. Podolske, S. E. Strahan, and K. R. Chan, A diagnostic for denitrification in the winter polar stratosphere, *Nature, 345,* 698–702, 1990.

Froidevaux, L., M. Allen, S. Berman, and A. Daughton, The mean ozone profile and its temperature sensitivity in the upper stratosphere and lower mesosphere: An analysis of LIMS observations, *J. Geophys. Res., 94,* 6389–6417, 1989.

Froidevaux, L., et al., Validation of UARS MLS ozone measurements, *J. Geophys. Res., 101,* 10,017–10,060, 1996.

Garcia, R. R., and S. Solomon, A numerical model of the zonally averaged dynamical and chemical structure of the middle atmosphere, *J. Geophys. Res., 88,* 1379–1400, 1983.

Jackman, C. H., R. S. Stolarski, and J. A. Kaye, Two-dimensional monthly average ozone balance from limb infrared monitor of the stratosphere and stratospheric and mesospheric sounder data, *J. Geophys. Res., 91,* 1103–1116, 1986.

Johnston, H. S., and J. Podolske, Interpretations of stratospheric chemistry, *Rev. Geophys., 16,* 491–519, 1978.

Jones, R. L., D. S. McKenna, L. R. Poole, and S. Solomon, On the influence of polar stratospheric cloud formation on chemical composition during the 1988/89 Arctic winter, *Geophys. Res. Lett., 17,* 545-548, 1990.

Jucks, K. W., D. G. Johnson, K. V. Chance, W. A. Traub, R. J. Salawitch, and R. A. Stachnik, Ozone production and loss rate measurements in the middle stratosphere, *J. Geophys. Res., 101,* 28,785–28,792, 1996.

Kawa, S. R., et al., Interpretation of NO_x/NO_y observations from AASE-II using a model of chemistry along trajectories, *Geophys. Res. Lett., 20,* 2507–2510, 1993.

Ko, M. K. W., N. D. Sze, and D. K. Weisenstein, The roles of dynamical and chemical processes in determining the stratospheric concentration of ozone in one-dimensional and two-dimensional models, *J. Geophys. Res., 94,* 9889–9896, 1989.

Kumer, J. B., et al., Comparison of correlative data with nitric acid data version v0007 from the cryogenic limb array etalon spectrometer (CLAES) instrument deployed on the NASA Upper Atmosphere Research Satellite (UARS), *J. Geophys. Res., 101,* 9621–9656, 1996.

Lahoz, W. A., et al., Validation of UARS MLS 183 GHz H_2O measurements, *J. Geophys. Res., 101,* 10,129–10,149, 1996.

Manney, G. L., R. W. Zurek, A. O'Neill, R. Swinbank, J. B. Kumer, J. L. Mergenthaler, and A. E. Roche, Stratospheric warmings during February and March 1993, *Geophys. Res. Lett., 21,* 813–816, 1994.

Manney, G. L., L. Froidevaux, J. W. Waters, R. W. Zurek, J. C. Gille, J. B. Kumer, J. L. Mergenthaler, A. E. Roche, A. O'Neill, and R. Swinbank, Formation of low-ozone pockets in the middle stratospheric anticyclone during winter, *J. Geophys. Res., 100,* 13,939–13,950, 1995.

McElroy, M. B., and R. J. Salawitch, Stratospheric ozone: Impact of human activity, *Planet. Space Sci., 37,* 1653–1672, 1989.

Mentall, J. E., J. E. Frederick, and J. R. Herman, The solar irradiance from 200 to 330 nm, *J. Geophys. Res., 86,* 9881–9884, 1981.

Mergenthaler, J. L., et al., Validation of CLAES $ClONO_2$ measurements, *J. Geophys. Res., 101,* 9603–9620, 1996.

Michelsen, H. A., et al., Stratospheric chlorine partitioning: Constraints from shuttle-borne measurements of HCl, $ClNO_3$, and ClO, *Geophys. Res. Lett., 23,* 2361–2364, 1995.

Morris, G. A., S. R. Kawa, A. R. Douglass, M. R. Schoeberl, J. Waters, and L. Froidevaux, Mid-stratospheric ozone loss in wave breaking events, *Eos Trans. AGU, 76(17),* Spring Meet. Suppl., S78, 1995.

Mount, G. H., and G. J. Rottman, The solar absolute spectral irradiance 1150-3173 Å: 17 May 1982, *J. Geophys. Res., 88,* 5403–5410, 1982.

Nair, H., M. Allen, G. L. Manney, R. Zurek, and L. Froidevaux, An investigation of low-ozone anomalies in the winter middle stratosphere using a Lagrangian photochemical model, *Eos Trans. AGU, 76(46),* Fall Meet. Suppl., F80, 1995.

Natarajan, M., L. B. Callis, R. E. Boughner, and J. M. Russell III, Stratospheric photochemical studies using Nimbus

7 data, 1, Ozone photochemistry, *J. Geophys. Res., 91,* 1153–1166, 1986.

Plumb, R. A, and M. K. W. Ko, Interrelationships between mixing ratios of long-lived stratospheric constituents, *J. Geophys. Res., 97,* 10,145–10,156, 1992.

Reber, C. A., C. E. Trevathan, R. J. McNeal, and M. R. Luther, The Upper Atmosphere Research Satellite (UARS) mission, *J. Geophys. Res., 98,* 10,643–10,647, 1993.

Roche, A. E., J. B. Kumer, J. L. Mergenthaler, G. A. Ely, W. G. Uplinger, J. F. Potter, T. C. James, and L. W. Sterritt, The cryogenic limb array etalon spectrometer (CLAES) on UARS: Experiment description and performance, *J. Geophys. Res., 98,* 10,763–10,775, 1993.

Roche, A. E., et al., Validation of CH_4 and N_2O measurements by the CLAES instrument on the Upper Atmosphere Research Satellite, *J. Geophys. Res., 101,* 9679–9710, 1996.

Siskind, D. E., B. J. Connor, R. S. Eckman, E. E. Remsberg, J. J. Tsou, and A. Parrish, An intercomparison of model ozone deficits in the upper stratosphere and mesosphere from two data sets, *J. Geophys. Res., 100,* 11,191–11,201, 1995.

Swinbank, R., and A. O'Neill, A Stratosphere-troposphere data assimilation system, *Mon. Weather Rev., 122,* 686–702, 1994.

Waters, J. W., et al., Validation of UARS MLS ClO measurements, *J. Geophys. Res., 101,* 10,091–10,127, 1996.

Woodbridge, E. L., et al., Estimates of total organic and inorganic chlorine in the lower stratosphere from in situ and flask measurements during AASE II, *J. Geophys. Res., 100,* 3057–3064, 1995.

World Meteorological Organization, Atmospheric Ozone 1985, *WMO Rep. 16,* Global Ozone Res. and Monit. Proj., Geneva, Switzerland, 1986.

M. Allen, L. Froidevaux, and R.W. Zurek, Earth and Space Sciences Division, Jet Propulsion Laboratory, California Institute of Technology, Pasadena, CA 91109. (e-mail: maa@mercu1.gps.caltech.edu; lucien@wilga.jpl.nasa.gov; rwz@rich.jpl.nasa.gov;)

H. Nair, Division of Geological and Planetary Sciences, California Institute of Technology, Pasadena, CA 91125. (e-mail: han@mercu1.gps.caltech.edu)

(Received April 3, 1997; revised October 7, 1997; accepted October 20, 1997.)